Orientation-dependent NMR study of the giant-unit-cell intermetallics β-Al_3Mg_2, Bergman-phase $Mg_{32}(Al,Zn)_{49}$, and ξ'-$Al_{74}Pd_{22}Mn_4$

P. Jeglič,[1] M. Komelj,[1] M. Klanjšek,[1] U. Tkalec,[1] S. Vrtnik,[1] M. Feuerbacher,[2] and J. Dolinšek[1]
[1]*J. Stefan Institute, University of Ljubljana, Jamova 39, SI-1000 Ljubljana, Slovenia*
[2]*Institut für Festkörperforschung, Forschungszentrum Jülich, Jülich D-52425, Germany*
(Received 12 October 2006; revised manuscript received 3 November 2006; published 3 January 2007)

We present a ^{27}Al NMR study of three giant-unit-cell complex metallic compounds, β-Al_3Mg_2, the "Bergman-phase" $Mg_{32}(Al,Zn)_{49}$, and ξ'-Al-Pd-Mn, which contain some hundreds up to more than a thousand atoms in the unit cell. The NMR spectra of monocrystalline samples are strongly inhomogeneously broadened by the electric quadrupole interaction and the line shapes are featureless and powderlike, but still exhibit significant orientation-dependent variation of the intensity on the satellite part of the spectrum in the magnetic field. Measuring orientation-dependent satellite intensity in appropriate frequency windows yields rotation patterns that can be related to the structure and symmetry of the giant unit cells. For a theoretical reproduction of the rotation patterns, we derived a distribution of the electric-field-gradient (EFG) tensors for each of the investigated compounds from existing structural models using point-charge and *ab initio* calculations. The EFG distribution yields important structural information on the manifold of different local atomic environments in the unit cell and distinguishes crystallographically inequivalent lattice sites from the equivalent ones. The distribution of the EFGs for the 1168-atom unit cell of β-Al_3Mg_2 was successfully determined by a point-charge calculation, whereas the *ab initio* approach was successful for the 160-atom unit cell of the $Mg_{32}(Al,Zn)_{49}$ Bergman phase. For the 258-atom unit cell of ξ'-Al-Pd-Mn, the experimental rotation patterns revealed a pseudotenfold symmetry, whereas the theoretical point-charge calculation revealed predominant twofold symmetry with traces of tenfold symmetry, so that no quantitative matching between the theory and experiment could be obtained.

DOI: 10.1103/PhysRevB.75.014202 PACS number(s): 61.44.Br, 76.60.−k

I. INTRODUCTION

The term "complex metallic alloys"[1] (CMAs) denotes exceptional intermetallic phases whose giant unit cells with lattice parameters of several nanometers contain from many tens up to several thousand atoms. Examples are the "Bergman-phase" $Mg_{32}(Al,Zn)_{49}$ with 162 atoms in the unit cell,[2] C_2-$Al_{39}Fe_2Pd_{21}$ (248 atoms/u.c.),[3] orthorhombic ξ'-$Al_{74}Pd_{22}Mn_4$ (258 atoms/u.c.)[4–6] and the related Ψ phase (about 1500 atoms/u.c.),[7] λ-Al_4Mn (586 atoms/u.c.),[8] cubic $NaCd_2$ (1152 atoms/u.c.),[9,10] cubic β-Al_3Mg_2 (1168 atoms/u.c.),[11,12] and the heavy-fermion compound $YbCu_{4.5}$, comprising as many as 7448 atoms in the supercell.[13] These giant unit cells contrast with elementary metals and simple intermetallics whose unit cells in general comprise from single up to a few tens of atoms only. The giant unit cells with lattice parameters of several nanometers provide translational periodicity of the CMA crystalline lattice on the scale of many interatomic distances, whereas on the atomic scale, the atoms are arranged in clusters with polytetrahedral order, where icosahedrally coordinated environments play the prominent role. The structures of CMAs thus show duality; on the scale of several nanometers, CMAs are periodic crystals, whereas on the atomic scale, they resemble quasicrystals (QCs).[14] A large group of CMAs is based on the 55-atom Mackay icosahedral cluster,[1] which is also the building block of icosahedral Al-Pd-Mn-type QCs.[14] Another group is based on the 105-atom Bergman cluster,[1,2] found also in icosahedral Mg-Al-Zn-type QCs.[15] While in the QC structure these clusters are distributed quasiperiodically, they are arranged on a periodic lattice in the CMAs.

A particular property of the CMA structures is the possibility of additional disorder in the giant unit cells apart from that due to atomic substitution, interstitials, or creation of vacancies, which are also present in simple intermetallics. In CMAs there exist also (i) *split* occupation, where two sites are alternatively occupied because they are too close in space to be occupied simultaneously and (ii) *configurational* disorder resulting from statistically varying orientations of a particular subcluster inside a given cage of atoms.

The structures of the giant-unit-cell CMA compounds can be described with reference to a six-dimensional hypercubic lattice in the framework of the cut-and-projection formalism[16] originally developed to describe QCs. The only difference is that a suitable rational cut is employed rather than an irrational one used for the QC lattice. For that reason the giant-unit-cell intermetallics are frequently referred to in the literature as rational approximants to QCs.

Due to the giant size of the unit cell, the structure determination of CMAs is a complicated task. X-ray crystallography is here an indispensable tool, whereas NMR spectroscopy can offer complementary structural information on the local atomic scale. Orientation-dependent NMR spectra of quadrupolar nuclei (such as ^{27}Al) in a magnetic field provide information on (i) the distribution of electric-field-gradient (EFG) tensors and the associated distribution of local atomic environments around the resonant nuclei, (ii) the number of crystallographically inequivalent lattice sites in the unit cell, and (iii) the local symmetry of the crystalline lattice. Moreover, we shall show that the orientation-dependent NMR spectra also reveal configurational disorder of a particular subcluster within the giant unit cell of a given CMA com-

pound. In this paper we present a ^{27}Al NMR study of three CMA compounds of increasingly larger unit cell and higher structural complexity: the $Mg_{32}(Al,Zn)_{49}$ Bergman phase with 162 atoms/u.c. (or 160 in the recently refined model by Sun *et al.*[17]), the ξ'-$Al_{74}Pd_{22}Mn_4$ (258 atoms/u.c.), and the β-Al_3Mg_2 (1168 atoms/u.c.).

II. NMR SPECTRUM

We derive first a theoretical ^{27}Al NMR spectrum applicable to nonmagnetic Al-based CMAs. In a metallic environment, the ^{27}Al nucleus (spin $I=5/2$) interacts with the surrounding ions and electrons by the electrical and magnetic interactions. The NMR resonance frequency corresponding to the $m \rightarrow m-1$ spin transition of the ith ^{27}Al nucleus in a magnetic field H_0 can be written as a sum[18,19]

$$\nu_i(m) - \nu_0 = \nu^{(1)}_{quad,i}(m) + \nu^{(2)}_{quad,i}(1/2) + \nu_{mag,i}, \tag{1}$$

where $\nu_0=\gamma_n H_0/2\pi$ is the Zeeman frequency and γ_n is the nuclear gyromagnetic ratio. The term $\nu^{(1)}_{quad,i}(m)$ is the first-order quadrupole shift that affects any spin transition $m \rightarrow m-1$, except the central $(1/2 \rightarrow -1/2)$ one,

$$\nu^{(1)}_{quad,i}(m) = -\frac{\nu_{Q,i}}{2}\left(m-\frac{1}{2}\right)(3\cos^2\theta_i - 1 + \eta_i \sin^2\theta_i \cos 2\phi_i). \tag{2}$$

The quadrupole coupling constant $\nu_{Q,i}=3e^2q^{(i)}Q/20h$ is determined by the largest principal value of the EFG tensor at the lattice site i, which can be written as[18]

$$V^{(i)}_{ZZ} = eq^{(i)} = V^{ion}_{ZZ,i}(1-\gamma^{(i)}_\infty) + V^{el}_{ZZ,i}. \tag{3}$$

The first term on the right-hand side of Eq. (3) originates from the neighboring ionic charges, enhanced by the Sternheimer antishielding factor $1-\gamma^{(i)}_\infty$ due to the ionic electric-field polarization of the core electrons, whereas the second term originates from the charges of the conduction electrons. The angles θ_i and ϕ_i in Eq. (2) describe the orientation of the applied magnetic field with respect to the principal-axes system (PAS) of the EFG tensor, and $\eta_i=(V^{(i)}_{XX}-V^{(i)}_{YY})/V^{(i)}_{ZZ}$ is the quadrupole asymmetry parameter. The first-order quadrupole shift is independent of the external magnetic field.

The second-order quadrupole shift is important only for the central transition, which is not affected by the quadrupole interaction in first order. It is inversely proportional to the external magnetic field and is written as

$$\begin{aligned}\nu^{(2)}_{quad,i}(1/2) = \frac{\nu^2_{Q,i}}{12\nu_0}\{&6\sin^2\theta_i(1-9\cos^2\theta_i) \\ &- 4\eta_i\cos 2\phi_i \sin^2\theta_i(9\cos^2\theta_i + 1) + \eta_i^2(-16/3 \\ &+ 8\cos^2\theta_i + 6\cos^2 2\phi_i \sin^4\theta_i)\}.\end{aligned} \tag{4}$$

The term $\nu_{mag,i}$ in Eq. (1) represents the frequency shift due to the magnetic hyperfine coupling between the nuclear spins and the conduction electrons. This shift is the same for all nuclear-spin transitions and is linearly proportional to the external field,

$$\nu_{mag,i} = \frac{\gamma_n}{2\pi}\left[K_i + \frac{K_{Z,i}}{2}(3\cos^2\theta'_i - 1 + \varepsilon_i \sin^2\theta'_i \cos 2\phi'_i)\right]H_0. \tag{5}$$

Here K_i is the isotropic Knight shift due to the contact interaction between the nucleus and the s electrons, whereas the parameters $K_{Z,i}$ and $\varepsilon_i=K_{X,i}-K_{Y,i}/K_{Z,i}$ are the largest principal value and the asymmetry parameter of the traceless anisotropic Knight-shift tensor that includes the dipolar interaction between the nucleus and the conduction electrons. The angles θ'_i and ϕ'_i describe the orientation of the magnetic field with respect to the PAS of the Knight-shift tensor.

Within the giant unit cell of a given CMA compound there exist generally many different local chemical environments. Consequently, there are many magnetically inequivalent resonant nuclei, each having its own set of the $V^{(i)}_{ZZ}$, η_i, K_i, $K_{Z,i}$, ε_i, θ_i, ϕ_i, θ'_i, and ϕ'_i parameters. The distribution of these parameters causes inhomogeneous broadening of the NMR spectrum, whereas their mean values shift its center of gravity. To obtain the spectrum $I(\nu)$ of a monocrystalline sample, we first integrate the frequency of each $m \rightarrow m-1$ transition over the distribution function g of these parameters. We get

$$F_m(\nu) = \int \delta[\nu - \nu(m)]g(V_{ZZ},\eta,K,K_Z,\varepsilon,\theta,\phi,\theta',\phi')d\Omega, \tag{6}$$

where $d\Omega$ is a differential of the phase space spanned by all the parameters in the distribution. For polygrain and powder samples one has to perform also the powder average over the random orientation of the grains. The spectrum is finally obtained by summing up all $F_m(\nu)$ contributions, weighted by their respective amplitudes of the nuclear-spin transitions $\beta_m=I(I+1)-m(m-1)$,

$$I(\nu) = \sum_{m=5/2}^{-3/2} \beta_m F_m(\nu). \tag{7}$$

The shape of the NMR spectrum, given by Eq. (7), depends crucially on the shape of the multiparameter distribution function g that contains parameters pertinent to both the electric quadrupole and the magnetic hyperfine interactions. We shall show that the width and shape of the satellite part of the ^{27}Al inhomogeneously broadened spectrum of the investigated CMAs are independent of the magnetic field, demonstrating that the first-order quadrupole interaction is by far dominant over the anisotropic Knight shift. This will allow us to make the following simplification: we shall assume that the magnetic shift of the spectrum can be described by a uniform shift K, describing the isotropic Knight shift, whereas the anisotropic Knight shift, which produces inhomogeneous broadening, can be neglected in comparison to the quadrupolar broadening. Within this approximation, the number of parameters in the distribution function g is reduced to four, so that $g(V_{ZZ},\eta,\theta,\phi)$ depends only on the parameters characterizing the EFG tensor magnitude and orientation.

In order to calculate the theoretical ^{27}Al NMR spectrum and its orientation dependence for a given CMA compound using Eq. (7), one has to introduce a model of the EFG distribution function $g(V_{ZZ}, \eta, \theta, \phi)$, which contains specific structural features of that compound. Below we perform this calculation for the β-Al_3Mg_2, the $Mg_{32}(Al,Zn)_{49}$ Bergman phase, and the ξ'-$Al_{74}Pd_{22}Mn_4$ CMAs using available structural models and compare the theoretical NMR rotation patterns to the experimental ones.

III. β-Al_3Mg_2

A. Structural details and sample characterization

According to the structural model by Samson,[11] the β-Al_3Mg_2 phase has an extraordinarily large face-centered cubic unit cell with space group $Fd\bar{3}m$ and a lattice constant a_0=2.82 nm. There are 1168 atoms in the unit cell. The local order can be described in terms of Friauf polyhedra, which arrange in slightly disordered icosahedral aggregates. Since a given atom may simultaneously belong to more than one polyhedron, a rather complex ordering network arises. The 1168 atoms are distributed over 23 crystallographically inequivalent sites, which, as a result of partial disorder (11 sites out of 23 are fractionally occupied), describe 41 different polyhedra. The unit cube contains 672 icosahedra, 252 Friauf polyhedra, and 244 miscellaneous, more-or-less irregular polyhedra of ligancy 10–16. About half the vertices of each icosahedron are occupied by magnesium atoms and the other half by aluminum atoms, providing very efficient packing of two kinds of atoms of different size around each central aluminum atom.

The sample was a monocrystal, grown by the Czochralski technique. It was shaped in the form of a rectangular prism with dimensions $2\times2\times7$ mm^3 and the long axis pointed along the [0 0 1] crystalline direction. Its chemical composition was determined using energy-dispersive x-ray spectroscopy (EDXS) to be $Al_{62.0}Mg_{38.0}$, corresponding to $Al_{3.26}Mg_2$, which is within the reported homogeneity range of the β phase[20] (extending from 37.5 to 40 at. % Mg). Structural studies by scanning-electron (SEM) and transmission-electron microscope (TEM) have shown[21] that the sample is a single-phase material with no inclusion of secondary phases. Bright-field TEM images[21] have revealed the presence of stacking-faultlike defects, as a consequence of thermal stresses during the cooling stage after growth. Physical properties of this sample (electrical resistivity, magnetic properties, thermal conductivity, and thermoelectric power) have been determined recently.[22] Electrical resistivity ρ exhibits a small positive temperature coefficient and the values $\rho_{4\ K}$=33.2 $\mu\Omega$ cm and $\rho_{300\ K}$=35.5 $\mu\Omega$ cm. Magnetic susceptibility χ is of Pauli type due to paramagnetism of conduction electrons. Thermoelectric power is small and negative, amounting to −2.8 μV/K at room temperature.

B. ^{27}Al Knight shift

The ^{27}Al NMR spectra of Al-based CMAs are generally strongly inhomogeneously broadened, and the spectral intensity extends over several MHz. Special techniques of field sweep and frequency sweep are needed to record such a spectrum. In our experimental setup we used one field-sweep spectrometer with the center field B_0=2.35 T and two frequency-sweep spectrometers, operating at fields 4.7 and 6.34 T. Their technical details, as well as the method of point-by-point scanning of the line, are described elsewhere.[19] A ^{27}Al field-swept NMR spectrum of the β-$Al_{3.26}Mg_2$ monocrystal, measured at a constant irradiation frequency $\nu(^{27}\mathrm{Al})$=26.053 MHz (corresponding to the ^{27}Al Larmor frequency in B_0=2.35 T) and a frequency-swept spectrum, measured in a constant field 6.34 T [corresponding to the Larmor frequency $\nu_0(^{27}\mathrm{Al})$=70.35 MHz] under identical conditions (T=80 K, [1 0 0] crystalline axis parallel to the field) are displayed superimposed in Fig. 1(a). The origin of the frequency axis is taken at the ^{27}Al resonance of the $AlCl_3$ aqueous solution and the spectra have been corrected for the uniform magnetic shift $\Delta\nu_m$ (the isotropic Knight shift, to be discussed in the following). The spectra extend over a frequency interval of about 1.2 MHz and show a typical spin I=5/2 structure. The broad "background" bell-like intensity corresponds to the first-order quadrupole-perturbed $\pm5/2\leftrightarrow\pm3/2$ and $\pm3/2\leftrightarrow\pm1/2$ satellite transitions, whereas the narrow, high-intensity line in the middle is the central line ($1/2\leftrightarrow-1/2$), quadrupole perturbed in second order. We observe that the satellite parts of the two spectra perfectly overlap and exhibit no field-dependent broadening, confirming that the first-order quadrupolar broadening dominates over the anisotropic Knight-shift broadening. While the quadrupolar shape of the orientation-dependent spectra will be discussed thoroughly in the following by employing the structural model of β-Al_3Mg_2, we discuss first the magnetic (Knight) shift of the spectrum, which was determined on the central line, where it is not masked by the large first-order quadrupole effect. The ^{27}Al frequency shift $\Delta\nu=\nu-\nu_{AlCl_3}$ of the central line was determined by the Fourier-transform technique (as the central lines are narrow, no sweeping is needed). The frequency shift is generally a sum of the second-order quadrupolar shift that scales inversely with the magnetic field B, $\Delta\nu_Q=a/B$, and the magnetic shift that is directly proportional to the field, $\Delta\nu_m=bB$. The opposite field dependences allow one to resolve $\Delta\nu_m$ and $\Delta\nu_Q$ by recording the frequency shift $\Delta\nu$ in two magnetic fields. In our experiments [Fig. 1(b)], the shifts of the central line in 2.35 and 4.7 T amounted to $\Delta\nu_{2.35\ T}$=36.4 kHz and $\Delta\nu_{4.7\ T}$=71.5 kHz. The ratio of the two shifts is $\Delta\nu_{4.7\ T}/\Delta\nu_{2.35\ T}$=1.96, which is almost exactly the ratio of the fields, 4.7 T/2.35 T=2.0, so that practically the entire shift is of magnetic origin; $\Delta\nu\approx\Delta\nu_m$. This yields the isotropic Knight shift $K=\Delta\nu_m/\nu_0=1.4\times10^{-3}$, which is close to the value in fcc Al (free-electronlike) metal where $K_{Al}=1.6\times10^{-3}$. The temperature dependence of the isotropic Knight shift was determined between 300 and 4 K in 4.7 T and is displayed in Fig. 1(c). The shift is temperature-independent within ±0.4%. Regarding the anisotropic Knight shift, we observe [Fig. 1(b)] that the full width at half height (FWHH) of the 2.35 T central line amounts to $\Delta\nu_{1/2}^{(2.35\ T)}$=13 kHz, whereas $\Delta\nu_{1/2}^{(4.7\ T)}$=20 kHz. The direct field dependence of this broadening shows that the magnetic broadening of the central line dominates over the second-order quadrupolar broadening.

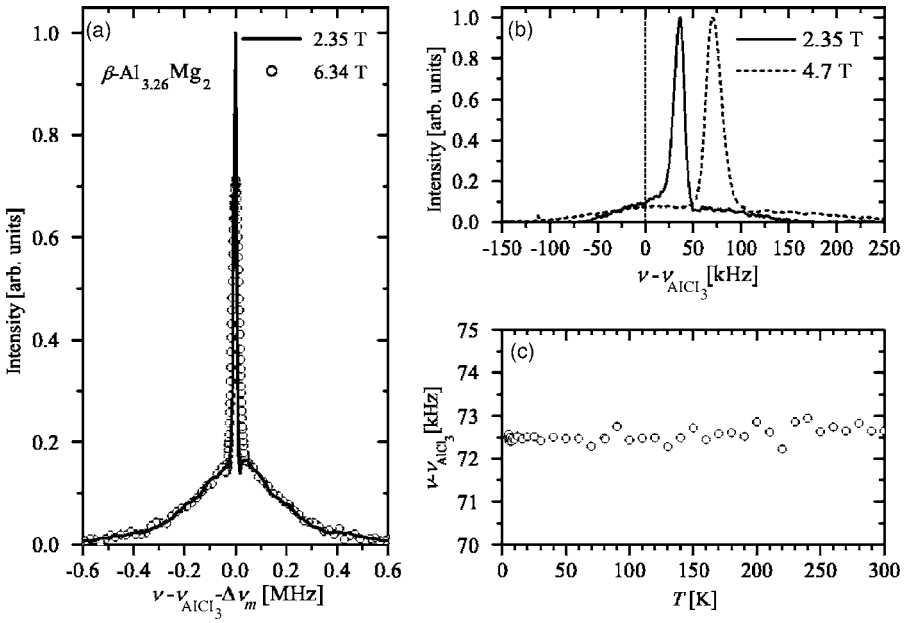

FIG. 1. (a) ^{27}Al field-swept NMR spectrum (solid line) of the β-$Al_{3.26}Mg_2$ monocrystal, measured at a constant irradiation frequency $\nu(^{27}\mathrm{Al})=26.053$ MHz and a frequency-swept spectrum (open circles), measured in a constant field 6.34 T at $T=80$ K and [1 0 0] axis parallel to the field. The spectra are normalized to the same integral. The origin of the frequency axis is taken at the ^{27}Al resonance of the $AlCl_3$ aqueous solution and the uniform magnetic shift $\Delta\nu_m$ (the isotropic Knight shift) has been subtracted. (b) Central lines in 2.35 and 4.7 T on an expanded frequency scale. The lines are obtained by a Fourier-transform technique and are scaled to the same height. (c) Temperature-dependent frequency shift of the central line in 4.7 T.

However, the width of the central line is small compared to its frequency shift (e.g., $\Delta\nu_{1/2}^{(4.7\ \mathrm{T})}=20$ kHz versus $\Delta\nu_{4.7\ \mathrm{T}}=71.5$ kHz), so that the anisotropic Knight shift is considerably smaller than the isotropic one. These figures justify neglecting the anisotropic Knight shift in comparison to the large first-order quadrupolar broadening (of about 1.2 MHz) in our theoretical calculation of the satellite part of the ^{27}Al NMR spectrum.

C. Orientation-dependent ^{27}Al NMR spectra

Apart from the trivial structure of a narrow central line superimposed on a broad satellite spectrum, the ^{27}Al NMR spectra of monocrystalline β-$Al_{3.26}Mg_2$ in Fig. 1(a) are featureless, resembling powder spectra of polycrystalline samples. It is tempting to see whether these spectra exhibit orientation dependence in a magnetic field. The large first-order quadrupolar broadening of the satellite spectrum suggests that the majority of the ^{27}Al nuclei occupy lattice sites with local symmetry lower than cubic, so that orientation dependence of the spectra is possible. In our rotation experiment, the crystal was rotated about the [0 0 1] crystalline axis, so that the magnetic field was rotated in the plane spanned by the [1 0 0] and [0 1 0] axes. The angle between the [1 0 0] and the magnetic field is labeled as β. All rotation patterns were performed at $T=80$ K in a magnetic field 6.34 T. In Fig. 2(a) we display two ^{27}Al frequency-swept spectra (normalized to the same integral), one with magnetic field parallel to [1 0 0] ($\beta=0$) and the other along [1 1 0] ($\beta=45°$). We observe that the satellite intensity exhibits small but significant orientation dependence. While the position of the full spectrum remains unchanged, the intensity varies over the spectrum upon rotation. Restricting our analysis to the high-frequency side of the symmetric spectrum (on the "right" of the central line), we observe that in the frequency range $70.50\ \mathrm{MHz}<\nu<70.55$ MHz the intensity of the $\beta=45°$ spectrum lies below that of the $\beta=0$ spectrum, whereas this becomes opposite in the frequency interval $70.65\ \mathrm{MHz}<\nu<70.9$ MHz. The crossover occurs at about 70.60 MHz, where the two intensities are equal. Figure 2(a) demonstrates the smallness of the differences in the orientation-dependent spectra (the spectra at the chosen orientations $\beta=0$ and 45° in fact exhibit the largest difference in one complete rotation run), so that it does not make much sense to compare the full spectra. Instead, a more illustrative way is to measure the spectral intensity in a chosen window (of 30 kHz width in our case) centered at a particular fixed frequency and plot the variation of this intensity as a function of the orientation. We have chosen four windows centered at frequencies 70.55, 70.60, 70.65, and 70.70 MHz [marked by vertical dashed lines in Fig. 2(a)]. The rotation pattern at 70.70 MHz (corresponding to the frequency where the difference between the $\beta=0$ and 45° spectra is the largest) in the interval $0<\beta<360°$ is displayed in Fig. 2(c). We observe a fourfold-symmetric pattern, consistent with the cubic symmetry of the unit cell. The rotation patterns at all chosen frequencies, restricted to the interval $0<\beta<90°$ due to the fourfold symmetry, are displayed in Fig. 2(d). The almost no orientation dependence at 70.60 MHz is due to the above-mentioned crossover of the intensities, which do not exhibit orientation dependence at this particular frequency.

In order to reproduce theoretically the rotation patterns of Fig. 2, we introduce the distribution function $g(V_{ZZ},\eta,\theta,\phi)$

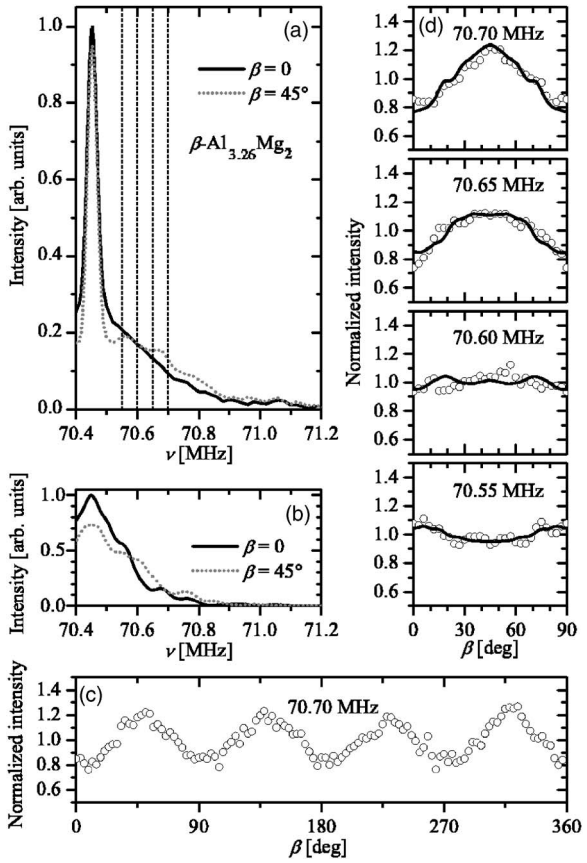

FIG. 2. (a) Two ^{27}Al frequency-swept NMR spectra of β-$Al_{3.26}Mg_2$ (normalized to the same integral) in a field 6.34 T and $T=80$ K at orientations $\beta=0$ (field parallel to [1 0 0]) and $\beta=45°$ (field along [1 1 0]). Vertical dashed lines indicate the frequencies at which the window-intensity rotation patterns were recorded. (b) Theoretical satellite parts of the spectra at $\beta=0$ and 45° obtained by a point-charge calculation on the Samson structural model[11] of β-Al_3Mg_2. (c) Rotation pattern around [0 0 1] of the window intensity at 70.70 MHz in one full rotation $0<\beta<360°$. (d) Rotation patterns around [0 0 1] of the window intensity in the interval $0<\beta<90°$ at the four frequencies indicated by vertical dashed lines in (a). Solid lines are theoretical fits described in the text.

of the EFG tensors at the Al sites pertinent to the β-Al_3Mg_2 structure. Our starting point is the structural model by Samson,[11] which we use to generate the giant unit cell of β-Al_3Mg_2 by a computer procedure suitable for further numerical calculations of the EFG tensors. Within this model, there are 23 crystallographically different atomic positions, out of which 11 are fractionally occupied. The total number of atomic sites in the unit cell is 1832, but only 1168 atoms can be actually accommodated, because groups of fractionally occupied sites are too close together to be occupied simultaneously (the criterion of shortest distance between neighboring atoms—amounting [11] to 2.5092 Å—would be violated). The fractional occupation makes a major problem in calculating the EFGs from the structural data; in a real unit cell, a given atomic site is either populated by an atom or vacant, but cannot contain "a fraction" of an atom with a fractional charge. To deal with this problem, we constructed the unit cell through the following steps. In the first step we have placed in the unit cell those atoms that sit on fully occupied lattice sites (occupation 1). These are the atoms Al(1), Al(2), Al(3), Al(5), Al(16), Al(22), Mg(4), Mg(6), Mg(15), Mg(17), Mg(18), and Mg(23) (the numbers refer to Table 1 Ref. 11). In the next step, these sites are multiplied according to the cubic space group $Fd\bar{3}m$ (No. 227). The so-obtained assembly of atoms (840 in total) provides a basis for all structural variants after the atoms at fractionally occupied sites are added. The next step is essential and involves building the clusters around eight Mg(23) atoms in the unit cell, which are surrounded by fractionally occupied sites only. The shortest-distance criterion allows the construction of two different polyhedra around a central Mg(23) atom: (1) a deformed centered pentagonal prism [Mg(23) +4Al(8)+4Al(10)] that has two additional Al(8) atoms above the base faces and (2) a tetrahedron [Mg(23) +12Al(7)+4Al(21)].

Inserting the prisms and tetrahedra into the unit cell, the space-group symmetry allows two arrangements, designated as mode 1 and mode 2. In mode 1 [Fig. 3(a)], the position (1/2,1/2,1/2) is occupied by a pentagonal prism, whereas in mode 2 [Fig. 3(b)] it is occupied by a tetrahedron. The tetrahedra in the two modes are oriented differently, but can have no configurational disorder within a given mode (mixing the two orientations within a given mode would violate the shortest-distance criterion). In contrast, the pentagonal prisms can assume six different orientations with equal probability (1/6) within a given mode and the orientations of different prisms in the unit cell are not correlated, i.e., the prisms can exhibit configurational disorder. A given prism can thus assume six orientations in two different environ-

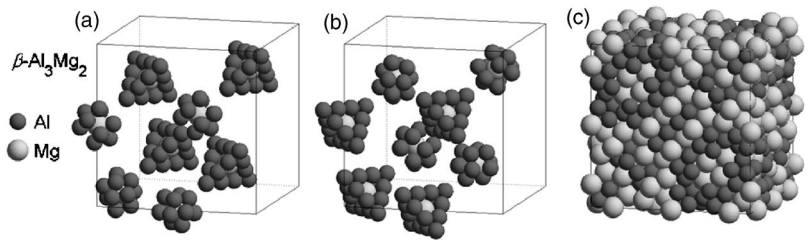

FIG. 3. Two arrangements [(a) mode 1 and (b) mode 2] of the pentagonal prisms and tetrahedra within the unit cell of β-Al_3Mg_2. While the tetrahedra can have no orientational disorder within a given mode, each pentagonal prism can assume six different orientations with equal probability, so that their sublattice contains inherent configurational disorder. In (c), one complete unit cell of β-Al_3Mg_2 (Samson model) is shown.

ments (mode 1 and mode 2), twelve settings altogether. Within the Samson model, this is accounted for by a twelfth-part fractional occupation of the four atomic sites Al(7), Al(8), Al(9), and Al(10), which surround a given central Mg(23) atom and are so close in space that only one can be populated at a time. Their respective populations are 6/12, 3/12, 2/12, and 1/12, which sum to 1. Here it is also important to note that, in real crystals, the domains of mode 1 and mode 2 structures can only coexist when being separated by domain walls; i.e., there exists no direct transformation from one domain to another. According to the average occupations of the atomic sites, each mode is occupied with 50% probability.

In the last step, the atoms at fractionally occupied sites Al(12), Al(14), Al(20), Mg(11), Mg(13), and Mg(19) are added. These adjust to the particular configuration allowed by the shortest-distance criterion, except Mg(19) that still has some freedom (already described by Samson[11]). In order not to violate the shortest-distance criterion at the cell borders, we have employed a periodic boundary condition by constructing a "supercell" (a complex of $3\times3\times3$ unit cells) that allowed control of the interatomic distances for all atoms within the central unit cell. All of the so-constructed structural variants of the unit cell comprise the same number of atoms, 1168 in total, with 720 Al and 448 Mg and the resulting average occupations of particular atomic sites equal to those of the Samson model. The complete unit cell is a dense close-packed structure [Fig. 3(c)], where the individual structural units (tetrahedra and pentagonal prisms) cannot be easily recognized. The existence of clusters as physical units in the β-Al_3Mg_2 structure is not obvious (the distances between the cluster atoms and the surrounding atoms are about the same), but grouping the atoms in clusters provides a convenient geometrical tool to describe the structure of the giant unit cell.

The next step is to calculate the distribution of the EFGs. A straightforward way is the *ab initio* calculation, but it is not feasible here due to the extreme size of the unit cell and the presence of fractionally occupied lattice sites. Instead, a model of dense packing of hard spheres and a point-charge calculation were shown to work well for close-packed solids with a large number of independent contributions to the EFG tensor, such as glasses, nanostructured materials, and icosahedral QCs.[23–25] A point-charge calculation of the EFG distribution was also successful in reproducing the orientation-dependent ^{27}Al NMR spectra of the decagonal $Al_{72.6}Ni_{10.5}Co_{16.9}$ QC,[19] so that we apply this method also to the β-Al_3Mg_2.

In our approximation we assign to all Al atoms the same dimensionless charge $+q$, whereas the charge of Mg atoms is set to $-(720/488)q$, in order to assure electrical neutrality of the unit cell. The actual q value is a fit parameter that finally rescales the theoretical NMR spectra to match the experimental ones. In the next step we generate a large set of unit cells starting with the atoms at fully occupied sites and then, using a random-generation procedure, fill the fractionally occupied sites one after another, always taking into account the shortest-distance criterion. In this way we obtain the whole statistical manifold of the possible variants of the unit cell, as described before. In the next step, the EFGs at the 720 Al sites are calculated in the crystal-fixed coordinate system (x,y,z) for each variant of the unit cell. Using a $3\times3\times3$ supercell, a sphere of 20 Å radius is drawn around each Al atom in the central unit cell and only the charges within this sphere are taken into account in the point-charge calculation (we have verified that an increased sphere radius does not change EFGs significantly any more). For the purpose of orientation-dependent NMR spectra, each EFG tensor is then transformed into the laboratory frame (x',y',z') chosen to have its z' axis parallel to the external magnetic field B, where it is diagonalized into its PAS [denoted as (X,Y,Z)] and the eigenvalues are labeled in the usual way as $|V_{XX}| \leqslant |V_{YY}| \leqslant |V_{ZZ}|$. The eigenvalue parameters V_{ZZ} and η and the orientation parameters θ and ϕ of the magnetic field with respect to the EFG PAS are then recorded and put into histograms. The so-obtained histogram of a given EFG parameter represents an integral of the joint distribution $g(V_{ZZ},\eta,\theta,\phi)$ over the other three parameters, i.e., it represents a particular marginal distribution of g. The histogram for V_{ZZ} represents the marginal distribution $f(V_{ZZ}) = \int g(V_{ZZ},\eta,\theta,\phi)d\eta\, d\theta\, d\phi$, whereas the histogram for η is $r(\eta) = \int g(V_{ZZ},\eta,\theta,\phi)dV_{ZZ}\, d\theta\, d\phi$. In a typical calculation run, about 100 unit cells are randomly generated. As each unit cell yields 720 Al EFG tensors, the total number of calculated EFGs is 10^5, assuring good statistics.

Once the distribution of the EFGs is obtained, we calculate the NMR spectrum $I(\nu)$ via Eq. (7) and then extract window intensities at frequencies corresponding to those of Fig. 2. In order to obtain theoretical rotation patterns of the window intensities, we choose initially the crystal (x,y,z) and the laboratory (x',y',z') frames to coincide and then rotate the crystal frame about the x' axis (that coincides with x), with β denoting the rotation angle. In Fig. 2(b) we display the theoretical satellite parts of the ^{27}Al spectra at $\beta=0$ and 45° orientations, corresponding to the experimental spectra of Fig. 2(a). The theoretical spectra reproduce well the features of the experimental ones (the two intensities cross at 70.60 MHz). The theoretical rotation patterns of the window intensities are displayed as solid lines in Fig. 2(d). The matching with experimental rotation patterns is excellent. The corresponding EFG distributions are displayed in Figs. 4 and 5. The marginal distribution $f(V_{ZZ})$ [Fig. 4(a)] resembles a discrete stick spectrum, whereas the $r(\eta)$ marginal distribution [Fig. 4(b)] also shows discretelike features, as it is peaked around several η values. This kind of shape of the V_{ZZ} and η distributions is a consequence of the fact that out of the 720 Al atoms in the unit cell, only a small number (14) of these are crystallographically different. The distribution of the EFG PAS orientations is best represented in a spherical plot, where the orientations of the V_{ZZ} principal direction in the crystal-fixed frame are shown on a sphere. In Fig. 5(a), the [1 0 0] crystalline axis points out of the graph from the middle of the sphere and the number (intensity) of the EFGs at a given orientation is denoted by a gray scale. A nice fourfold-symmetric pattern is observed. In Fig. 5(b), the same distribution is viewed along the [1 1 1] crystal direction, showing now the threefold symmetry of the cubic space group of β-Al_3Mg_2. In Figs. 5(c) and 5(d), the orientational distributions of the V_{YY} and V_{XX} principal directions viewed

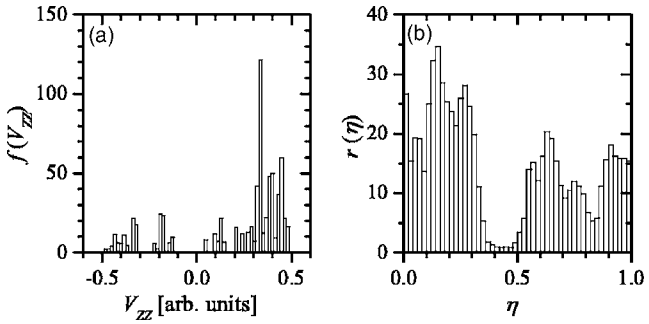

FIG. 4. Marginal distributions (a) $f(V_{ZZ})$ and (b) $r(\eta)$ of the ^{27}Al EFG-tensor eigenvalues in the unit cell of β-Al_3Mg_2, calculated from the Samson model and used for the theoretical reproduction of the orientation-dependent NMR window intensities [solid lines in Fig. 2(d)].

along [1 0 0] are shown, respectively. Also there, the fourfold symmetry is evident.

The above experimental and theoretical study shows that the strongly inhomogeneously broadened ^{27}Al NMR spectra of the β-Al_3Mg_2 monocrystalline sample, though hopelessly featureless and powderlike at a first glance, contain valuable structural information, which can be best extracted from the rotation patterns of the spectral intensities in different windows on the first-order quadrupole-perturbed satellite part of the NMR spectrum. Rotation patterns exhibit symmetry that reveals the macroscopic symmetry of the unit cell. A theoretical distribution of the EFG tensors is calculated from the existing structural model and is then used to reproduce the rotation patterns. The NMR rotation patterns can thus prove (disprove) a given structural model of a giant-unit-cell CMA compound. The theoretical and experimental rotation patterns of β-Al_3Mg_2 confirm that, out of the 720 Al EFG tensors in one unit cell, only a small number possess different

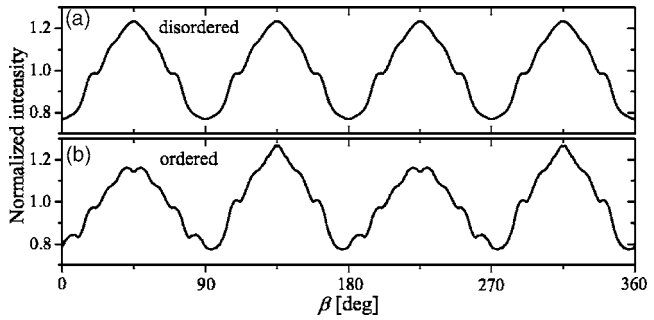

FIG. 6. Theoretical rotation patterns of the window intensity at 70.70 MHz [corresponding to Fig. 2(c)] for two cases: (a) the model of configurationally disordered pentagonal prisms and (b) the ordered model, where all prisms assume the same orientation.

eigenvalues (corresponding to fourteen crystallographically inequivalent Al sites), whereas their orientations point into many different, but still finite in number, groups of solid angles on a sphere. This is consistent with the crystalline nature of the β-Al_3Mg_2 structure, which shows no resemblance to random structures like glasses and amorphous phases, where EFGs would be distributed more or less continuously (probably by a Gaussian distribution) in both magnitude and orientation.

A final issue to comment on is the sensitivity of the NMR window-intensity rotation patterns to the configurational disorder of pentagonal prisms in the β-Al_3Mg_2 unit cell. It is this configurational disorder that leads to the average cubic $Fd\bar{3}m$ symmetry of the β-Al_3Mg_2 structure, whereas without the configurational disorder, the cubic symmetry would be lost. In Fig. 6 we display theoretical rotation patterns [corresponding to that of Fig. 2(c)] of the window intensity for two cases: (i) the model of configurationally disordered prisms (equal to the model considered so far) and (ii) the ordered

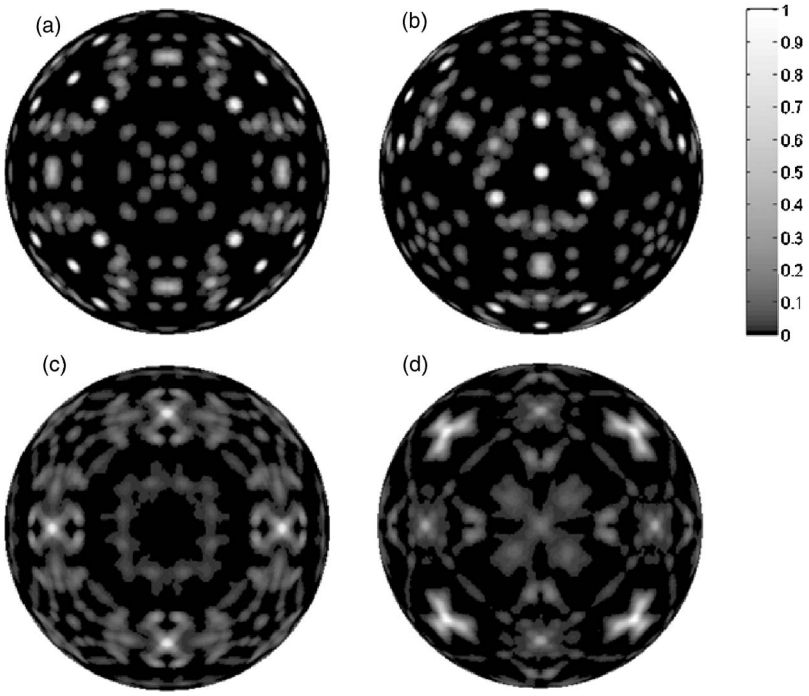

FIG. 5. The distribution of the EFG PAS orientations in the crystal-fixed frame of β-Al_3Mg_2 represented in a spherical plot, where the orientations of the V_{ZZ} principal direction are shown on a sphere. In (a), the [1 0 0] crystalline axis points out of the graph and the number (intensity) of the EFGs is denoted by a gray scale, whereas in (b), the same distribution is viewed along [1 1 1]. In (c) and (d), the orientational distributions of the V_{YY} and V_{XX} principal directions are shown, respectively, where the [1 0 0] direction points out of the graphs.

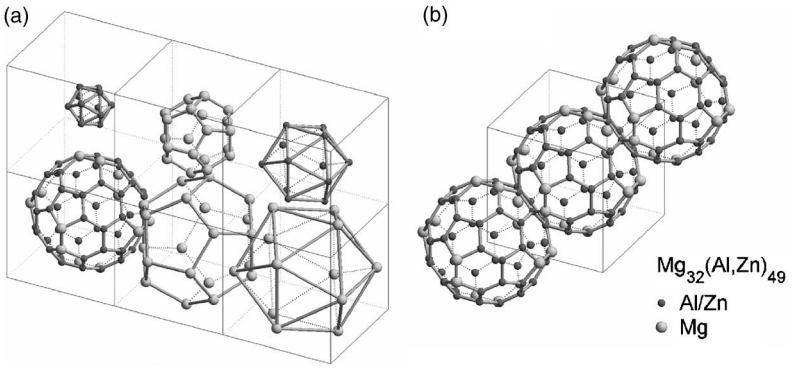

FIG. 7. (a) Six successive shells of the Bergman icosahedral cluster (see text). (b) The structure of the Bergman phase is obtained by a body-centered packing of these clusters by sharing a hexagonal plane of the fourth shell (the soccer ball).

model, where all prisms would assume the same orientation. We observe that the fourfold symmetry of the disordered model [Fig. 6(a)] is lost in the ordered model [Fig. 6(b)], which shows only a twofold-symmetric pattern. Since the experimental rotation pattern in Fig. 2(c) is fourfold symmetric, this supports the presence of configurational disorder on the sublattice of pentagonal prisms.

IV. $Mg_{32}(Al,Zn)_{49}$ BERGMAN PHASE

A. Structural details and sample characterization

The structure of the Bergman-phase $Mg_{32}(Al,Zn)_{49}$ was first solved in 1957 by Bergman *et al.*[2], whereas a refinement of the structure was reported recently by Sun *et al.*[17] The unit cell is cubic with space group $Im\bar{3}$, and contains 162 atomic sites. The Bergman phase can exist in a wide compositional region in the Mg-Al-Zn phase diagram,[26] in contrast to the thermally stable icosahedral QCs that can form only in a narrow compositional range[27] around $Mg_{44}Al_{15}Zn_{41}$. Within the homogeneity range of the Bergman phase, the lattice constant was reported[17] to vary between $a=1.4194$ and 1.4459 nm for increasing Zn content between 14 and 51 at. %. The basic element of the structure is the Bergman icosahedral cluster consisting of six successive shells [Fig. 7(a)]. From the center these shells are (1) an icosahedron, (2) a pentagonal dodecahedron, (3) a larger icosahedron, (4) a truncated icosahedron (a "soccer ball" structure), (5) a larger pentagonal dodecahedron, and (6) an even larger icosahedron. The final structure is obtained by a body-centered packing of these clusters [Fig. 7(b)] by sharing a hexagonal plane of the fourth shell (the soccer ball). Eight crystallographically different atomic sites were identified in the unit cell. The coordination polyhedra around these sites have ligancy 12 (icosahedron), 14, 15, and 16 (Friauf polyhedron). All of the zinc and aluminum atoms in the unit cell have icosahedral coordination. The only difference between the original structure by Bergman *et al.*[2] and the refined one by Sun *et al.*[17] is that the refined structure does not have an atom in the center of the cluster. Consequently, the unit cell of the Bergman model contains 162 atoms, whereas there are 160 atoms in the model by Sun with all sites fully occupied (occupancy 1). No fractional occupation is, therefore, present in the Sun model of the Bergman phase. As Zn directly replaces Al, the Al/Zn sites possess inherent chemical disorder and the ratio of the Al-to-Zn occupation of each site is different, depending also on the Zn concentration in the crystal. In our calculation of the EFG distribution we shall be using the model by Sun. Here it is worth mentioning that the existence of the central atom in the cluster is still a matter of debate. While in the model by Sun[17] this site remains unoccupied within the investigated compositional range 14–51 at. % Zn, Mizutani *et al.*[28] have reported that this site is vacant in the range 15–25 at. % Zn, whereas it becomes occupied by Al atoms up to a ~10% occupancy as Zn content increases beyond 30 at. %.

The sample material was grown by the Czochralski technique and the details of its growth, structural characterization, and physical properties (electrical resistivity, magnetic properties, thermal conductivity, and thermoelectric power) are reported elsewhere.[29] The sample for measurements was cut from a Czochralski monocrystalline ingot and was shaped in the form of a rectangular prism with dimensions $2\times2\times7$ mm^3 and the long axis was parallel to the [0 0 1] crystalline direction. The chemical composition, in at. %, was $Mg_{36.3}Al_{32.0}Zn_{31.7}$ [corresponding to $Mg_{29.4}(Al,Zn)_{51.6}$, which is within the homogeneity range of the Bergman phase[26]]. The SEM backscattered-electron (BSE) image showed a featureless, homogeneous pattern, confirming that the sample consists of a single phase with no inclusion of secondary phases. The investigated sample possesses the following physical properties:[29] electrical resistivity exhibits a small positive temperature coefficient and the values $\rho_{4\ K}=40.6\ \mu\Omega$ cm and $\rho_{300\ K}=46.8\ \mu\Omega$ cm; magnetic susceptibility χ is of a Pauli type due to paramagnetism of conduction electrons and the thermoelectric power is small and negative, amounting to $-5\ \mu$V/K at room temperature.

B. The ^{27}Al Knight shift

The ^{27}Al NMR spectrum of the monocrystalline $Mg_{29.4}(Al,Zn)_{51.6}$ Bergman-phase sample [Fig. 8(a)] is similar to that of the previously discussed β-Al_3Mg_2. The same structure of a narrow central line and broad satellite intensity applies, where the first-order quadrupole-perturbed satellites extend here over a 1.6 MHz interval. In a rotation pattern in a magnetic field, the intensity on the satellite part of the spectrum exhibits significant orientation dependence. In Fig. 8(a), three ^{27}Al spectra, measured by a frequency-sweep technique in a field 6.34 T and $T=80$ K in a rotation about the [0 0 1] crystalline axis, are displayed at orientations $\beta=0$, 111°, and 147°. These spectra show boundaries of the

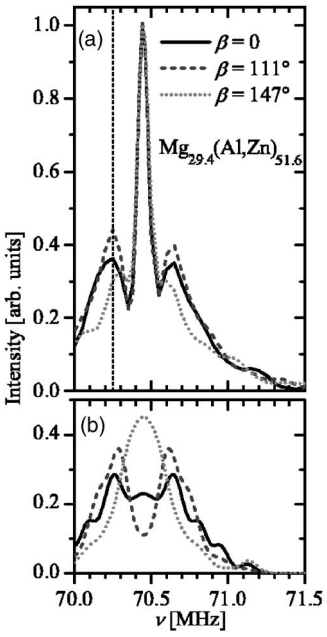

FIG. 8. (a) ^{27}Al frequency-swept NMR spectra of monocrystalline $Mg_{29.4}(Al,Zn)_{51.6}$ Bergman-phase sample at 80 K and orientations $\beta=0$, 111°, and 147°. The dashed vertical line indicates the frequency at which the window-intensity rotation patterns were recorded. (b) Theoretical reproduction of the same spectra (the satellite parts are shown only) by the *ab initio* calculation (see text).

intensity variation in one complete rotation run. Like before, the $\beta=0$ orientation corresponds to the [1 0 0] axis parallel to the field.

The ^{27}Al Knight shift was determined on the central line using the same procedure as already described for β-Al_3Mg_2. The central lines for the $\beta=0$ orientation at 80 K in two magnetic fields 2.35 and 4.7 T are displayed in Fig. 9(a). The frequency shifts relative to the $AlCl_3$ aqueous solution amount to $\Delta\nu_{2.35\ T}=27$ kHz and $\Delta\nu_{4.7\ T}=59$ kHz. Decomposition of the total shift into the quadrupolar and magnetic contributions, $\Delta\nu=\Delta\nu_Q+\Delta\nu_m=a/B+bB$, yielded $a=-7.8$ kHz T and $b=12.9$ kHz/T, so that $\Delta\nu_Q^{2.35\ T}=-3.3$ kHz and $\Delta\nu_m^{2.35\ T}=30.3$ kHz, whereas $\Delta\nu_Q^{4.7\ T}=-1.6$ kHz and $\Delta\nu_m^{4.7\ T}=60.6$ kHz. The magnetic shift thus dominates over the second-order quadrupolar shift and yields the isotropic Knight shift $K=\Delta\nu_m/\nu_0=1.16\times10^{-3}$. The temperature dependence of the isotropic Knight shift was determined between 300 and 4 K in a magnetic field 4.7 T and is displayed in Fig. 9(b). The shift is constant from 4 to 150 K, whereas it exhibits a tiny increase by about 3% (from 59 kHz at 150 K to 61 kHz at 300 K) at higher temperatures. Regarding the anisotropic Knight shift, the situation is analogous to that of β-Al_3Mg_2. The central line exhibits predominantly magnetic broadening, but its FWHH—a measure of the anisotropic Knight shift—is considerably smaller than the isotropic Knight shift (i.e., $\Delta\nu_{1/2}^{(4.7\ T)}=31$ kHz versus $\Delta\nu_{4.7\ T}=59$ kHz). These figures again justify neglecting the anisotropic Knight shift in comparison to the large first-order quadrupolar broadening (of about 1.6 MHz) when analyzing the satellite part of the ^{27}Al NMR spectrum.

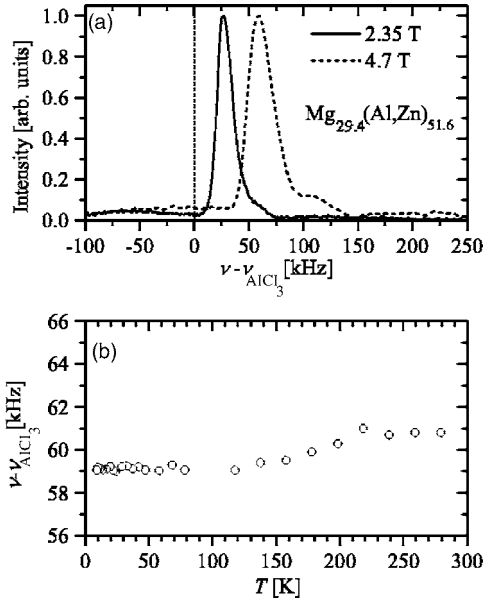

FIG. 9. (a) Central lines of the ^{27}Al NMR spectra of $Mg_{29.4}(Al,Zn)_{51.6}$ for the $\beta=0$ orientation at 80 K in two magnetic fields 2.35 and 4.7 T. The lines are obtained by a Fourier-transform technique and are scaled to the same height. (b) Temperature-dependent frequency shift of the central line in 4.7 T.

C. Orientation-dependent ^{27}Al NMR spectra

Orientation-dependent spectra were measured under identical conditions as those of β-Al_3Mg_2 ($T=80$ K, magnetic field 6.34 T and the frequency-sweep scanning technique). The frequency window for measurements (of width 30 kHz) was chosen at 70.25 MHz [marked by a vertical dashed line in Fig. 8(a)], where the intensity variation with orientation is the largest. We have recorded several rotation patterns by systematically changing the axis of rotation within the (y,z) plane of the crystal-fixed frame in steps of 15°. We denote by φ the angle between the rotation axis and the [0 0 1] direction, so that $\varphi=0$ corresponds to rotation about [0 0 1] and $\varphi=90°$ to rotation about [0 1 0]. The seven recorded rotation patterns (at $\varphi=0$, 15°, 30°, 45°, 60°, 75°, and 90°) are displayed in Fig. 10(a). The rotation patterns exhibit twofold symmetry, where the angle $\beta=90°$ represents a plane of mirror symmetry. The absence of fourfold symmetry in the rotation patterns is not in contradiction with the $Im\bar{3}$ (No. 204) space group of $Mg_{32}(Al,Zn)_{49}$. Though the unit cell is cubic, atomic decoration within the cell is such that fourfold symmetry is absent.

As compared to β-Al_3Mg_2, the theoretical calculation of the EFG distribution for the $Mg_{32}(Al,Zn)_{49}$ Bergman-phase unit cell is facilitated by three facts: (i) the number of atoms in the unit cell (160) is relatively small in comparison to β-Al_3Mg_2 (1168), (ii) there are no fractionally occupied sites within the unit cell, and (iii) due to full occupation of the atomic sites, there is no problem with the shortest-distance criterion (amounting here[17] to 2.539 Å), when constructing the unit cell for the EFG calculations. Under these conditions, the *ab initio* approach of calculating atomic charges and EFGs is feasible and we used that method for the Bergman phase.

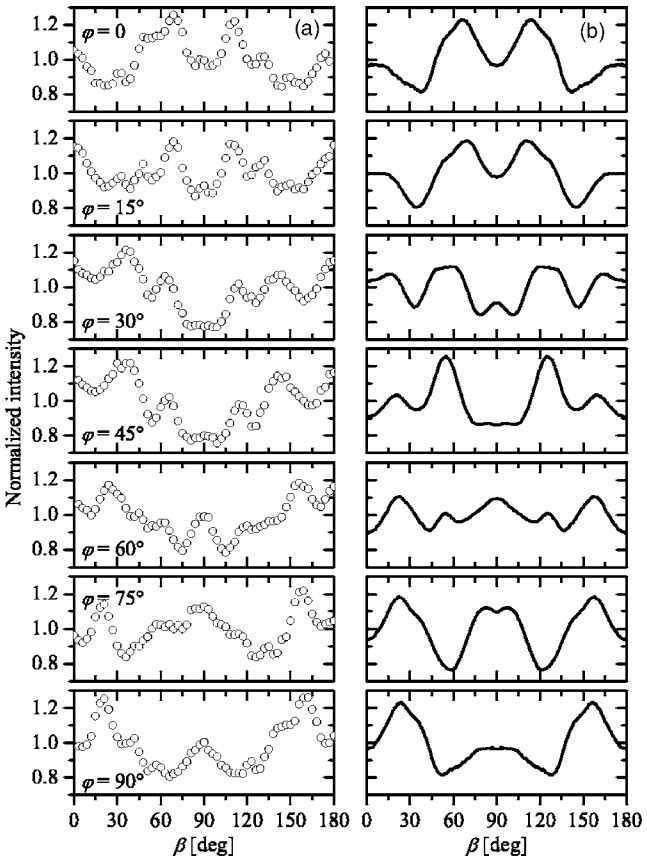

FIG. 10. (a) Experimental rotation patterns of the ^{27}Al window intensity at the frequency 70.25 MHz [marked by the vertical dashed line in Fig. 8(a)] for seven different axes of rotation within the (y,z) plane of the crystal-fixed frame. φ denotes the angle between the rotation axis and the [0 0 1] direction, so that $\varphi=0$ corresponds to rotation about [0 0 1] and $\varphi=90°$ to rotation about [0 1 0]. In (b), the theoretical rotation patterns, obtained by *ab initio* calculation on an Al-Mg-Al unit cell, are displayed side by side with the experimental ones.

The *ab initio* calculations were performed within the framework of the density-functional theory (DFT) and the local-density approximation (LDA).[30] The calculation of atomic charges and the EFG-tensor components[31] was performed by applying the WIEN97 code,[32] which adopts the full-potential linearized-augmented-plane-waves (FLAPW) method.[33] The cut-off energy for the basis set was 85 eV, and the number of **k** points in the full Brillouin zone was 64, which is, according to the convergency tests, sufficient for a reliable calculation of the EFGs. Within the FLAPW method, the considered supercell of $3\times3\times3$ unit cells is divided into the muffin-tin (MT) spheres centered at particular atoms, and the interstitial region. The calculated atomic charges, which are obtained as the integrals of the corresponding charge densities within the particular MT spheres, depend slightly on the MT radia. We have set the MT radia for all sites and elements to 2.395 (in arb. units). A change of the calculated atomic charges due to a reasonable variation of this value is below the required accuracy for the application of the point-charge model. The criterion for the self-consistency of the calculated charge density was the difference in the total energy after the last two iterations being less than 1×10^{-4} Ry.

TABLE I. *Ab initio*-calculated eigenvalue V_{ZZ} and the asymmetry parameter η of the EFG tensors at the Al sites in the unit cell of the Bergman phase. V_{ZZ} is obtained in absolute units with no adjustable parameter involved in the calculation. Atomic sites are labeled according to the nomenclature by Sun *et al.*[17] The quadrupole coupling constant ν_Q is given also.

Site: atom	V_{ZZ} (10^{21} V/m^2)	η	ν_Q (MHz)
B: Al	−0.722	0.047	−0.383
C: Al	0.684	0.980	0.363
F: Al	−0.691	0.329	−0.366

The calculation proceeds as follows. In principle we would have to construct a large number of unit cells with different Al/Zn decorations and perform *ab initio* calculation of the EFGs on each of these. The $Im\bar{3}$ symmetry is valid only for a statistical manifold of such unit cells and does not hold for a single Al-Mg-Zn unit cell. To avoid this large computational task, we made the following approximation. Taking into account that Al and Zn directly replace each other, we replace all Zn atoms by Al and consider an Al-Mg-Al unit cell instead of an Al-Mg-Zn. The advantage is that now already a single Al-Mg-Al unit cell obeys the $Im\bar{3}$ symmetry, so that *ab initio* is performed on just one cell. The Al-Mg-Al unit cell contains 96 Al atoms on three crystallographic sites ($24B+24C+48F$, using the nomenclature of Table 1 by Sun[17]) and 64 Mg atoms ($16D+24E+12G+12H$). Since there are only three inequivalent Al atoms in the unit cell, only three EFG tensors have different eigenvalues (Table I). Different orientations of these tensors in the crystal-fixed frame are obtained by applying $Im\bar{3}$ space-group symmetries, yielding in total 24 EFG tensors in one unit cell. Once the *ab initio*-calculated EFG tensors are available, the orientation-dependent NMR spectra and the window intensity are calculated in the same way as explained for the β-Al_3Mg_2. In Fig. 8(b) we display the theoretical spectra at $\beta=0$, 111°, and 147° for the [0 0 1] ($\varphi=0$) rotation (only the satellite parts of the spectra are shown) that are to be compared to the experimental spectra of Fig. 8(a). The two sets of spectra show reasonable matching with regard to the orientation-dependent shape and intensity variation. In Fig. 10(b), the theoretical rotation patterns of the window intensity for all seven rotation axes are shown side by side with the experimental ones [Fig. 10(a)]. For some rotation axes, the agreement between the theory and experiment is excellent (compare, e.g., the theoretical and experimental patterns at $\varphi=0$, 75°, 90°), whereas at other orientations, the agreement is still qualitatively correct by reproducing local minima and maxima, but not their relative intensities (the fact that the accuracy of the angle φ setting was ±3° may add to this discrepancy). The corresponding marginal distributions $f(V_{ZZ})$ and $r(\eta)$ are displayed in Figs. 11(a) and 11(b), showing a discrete stick spectrum due to three-only inequivalent Al sites in the unit cell. The distribution of orientations of the V_{ZZ} principal direction in the crystal-fixed

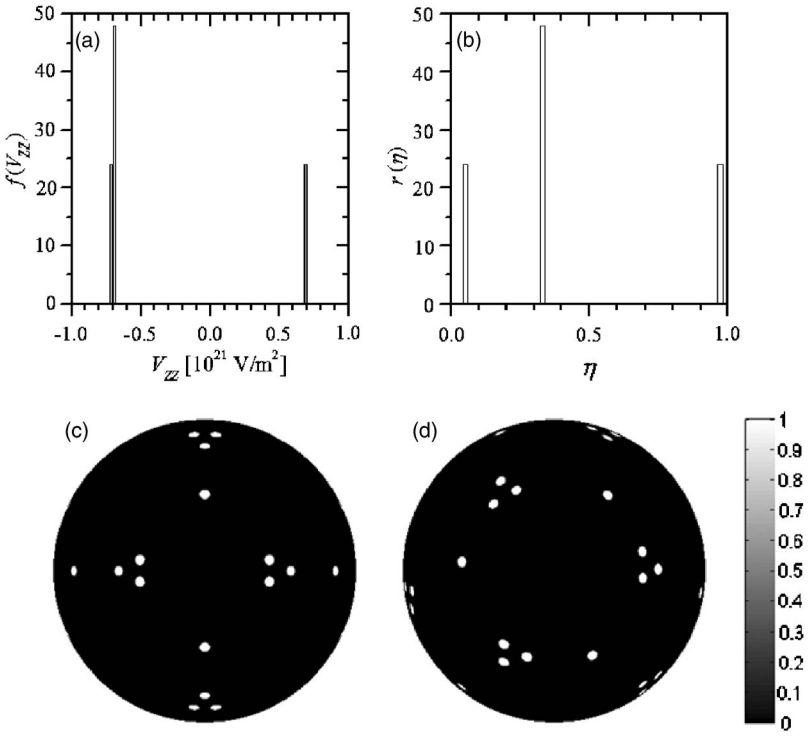

FIG. 11. Marginal distributions (a) $f(V_{ZZ})$ and (b) $r(\eta)$ of the ^{27}Al EFG-tensor eigenvalues for an Al-Mg-Al unit cell of the Bergman phase, calculated from the Sun model[17] and used for the theoretical reproduction of the orientation-dependent window intensities in Fig. 10(b). In (c), the distribution of orientations of the V_{ZZ} principal direction in the crystal-fixed frame is shown in a spherical plot as viewed along the [1 0 0] crystalline direction, whereas in (d), the same distribution is viewed along [1 1 1].

frame is shown by spherical plots in Figs. 11(c) and 11(d). In Fig. 11(c), the [1 0 0] crystalline axis points out of the graph, whereas in Fig. 11(d), the same distribution is viewed along [1 1 1]. As already discussed, there is no fourfold symmetry along [1 0 0] for the $Im\bar{3}$ space group, but only twofold symmetry, which is also a feature of the distribution shown in Fig. 11(c). A threefold symmetry is evident along [1 1 1] in Fig. 11(d).

It is also worth noting that the *ab initio*-calculated V_{ZZ} eigenvalues from Table I, which are obtained in absolute units with no adjustable parameter involved in the calculation, reproduce well also the total width of the experimental ^{27}Al NMR spectrum from Fig. 8(a) that extends over about 1.6 MHz. Using the electric quadrupole-moment value of the ^{27}Al nucleus $Q=0.146\times10^{-24}$ cm^2, the quadrupole coupling constants $\nu_Q=3eV_{ZZ}Q/20h$ are calculated in Table I (giving the values of $|\nu_Q|\approx0.37$ MHz). The spectral intensity of a spin $I=5/2$ nucleus generally extends over $4\nu_Q$, which yields a theoretical width $4\nu_Q\approx1.5$ MHz that matches well to the experimental value of 1.6 MHz.

Finally, we compared the *ab initio* approach of calculating the EFGs to the point-charge calculation on dense packing of hard spheres, as successfully applied to β-Al_3Mg_2. We have assumed Al and Mg valences to be those obtained from the *ab initio* calculation and conducted the full point-charge calculation of the window-intensity rotation pattern for the $\varphi=0$ rotation along the same steps as in the case of β-Al_3Mg_2. The result is displayed in Fig. 12(c), together with the experimental pattern [Fig. 12(a)] and the *ab initio* pattern [Fig. 12(b)]. We observe that, while the *ab initio* result more or less perfectly matches the experimental one, the point-charge calculation on hard spheres fails, yielding much more structured and spiky rotation pattern that has little (or no) resemblance to the experimental pattern. This indicates the inadequacy of the hard-sphere point-charge model for the $Mg_{32}(Al,Zn)_{49}$ Bergman phase. The reason for the failure is very likely improper treatment of the conduction-electron charge density in the EFG calculation, which is in a conducting solid smeared over the crystal and not concentrated at lattice points, as assumed by the point-charge model. The same problem should be, in principle, present also in the case of β-Al_3Mg_2, but astonishingly does not appear there. Though we have no definite answer for the reason of success of the point-charge approach for β-Al_3Mg_2, the considerably larger unit cell seems to be in favor of the point-charge calculation. Another possibility, still to be verified, is that the

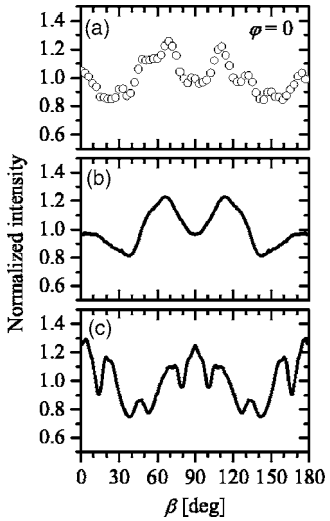

FIG. 12. Comparison of (a) the experimental window-intensity rotation pattern for the $\varphi=0$ rotation with the theoretical patterns calculated by (b) the *ab initio* method and (c) the point-charge calculation.

conduction-electron cloud in β-Al_3Mg_2 is to some extent confined to atomic clusters, making it more localized and point-chargelike.

V. ξ'-$Al_{74}Pd_{22}Mn_4$

A. Structural details and sample characterization

According to the structural model by Boudard *et al.*,[4] the ξ'-Al-Pd-Mn structure is described in terms of an orthorhombic unit cell with space group *Pnma* (No. 62) and the lattice parameters[4,5] $a=2.354$ nm, $b=1.656$ nm, and $c=1.234$ nm. There are 320 atomic sites within the giant unit cell, out of which about 258 are occupied on average (183 Al, 59 Pd, and 16 Mn) due to the fractional occupation of many of the sites. Several sites also possess Al/Pd or Al/vacancy substitutional disorder. The chemical composition of the compound is about $Al_{74}Pd_{22}Mn_4$. The skeleton of the unit cell is well understood and is built up of atomic clusters of the distorted pseudo-Mackay icosahedra, whereas the intermediate space is less clear and contains considerable disorder. A pseudo-Mackay cluster is built around the central Mn(12) atom, which is surrounded by a half-populated small pentagonal dodecahedron of Al atoms[34] (about 10 out of 20 atomic sites are populated on average) and an outer shell of two interpenetrating clusters, an icosahedron of 12 Pd atoms and an icosidodecahedron of 30 Al atoms. It is not clear why some lattice sites within the skeleton [i.e., Al(1)–Al(9)] are only partially occupied, though they are remote enough in space to be occupied simultaneously. The central Mn(12) atoms of the pseudo-Mackay clusters form a two-dimensional lattice of flattened hexagons in a plane perpendicular to [0 1 0] direction. The hexagons are arranged in a "herringbone" manner and there exist two such planes within the unit cell (at $y=0$ and $1/2$). The decorated flattened-hexagon lattice is presented in Fig. 13(a) in a view along [0 1 0], whereas in Fig. 13(b), a perpendicular view is shown. Other atomic layers perpendicular to [0 1 0] can be defined,[4] so that the ξ'-Al-Pd-Mn structure is described as a stacked-layer structure with three different flat and one puckered layer located at 0, 0.12, 0.16, and 0.25 fractional y coordinate, each of them exhibiting local pentagonal symmetry about the [0 1 0] axis.

An interesting geometrical feature of the flattened-hexagon lattice of ξ'-Al-Pd-Mn is that it can be alternatively described as a tiling of two rhombohedral tiles (a "skinny" and a "fat" one), i.e., it can be represented as a periodic approximant to the two-dimensional Penrose tiling. This is indicated in Fig. 13(a), where one flattened hexagon is decomposed into two "fat" and one "skinny" tile by dashed lines. The smaller inner angles of the two kinds of tiles are close to the ideal Penrose values 36° and 72°, respectively.

It is also worth noting that very similar pseudo-Mackay-type local icosahedral order is present also in the icosahedral *i*-Al-Pd-Mn quasicrystalline phase, making the giant-unit-cell ξ'-Al-Pd-Mn an excellent periodic approximant to the icosahedral phase. While in the *i*-Al-Pd-Mn phase the pseudo-Mackay icosahedra are distributed hierarchically on a quasiperiodic lattice, they are arranged on a periodic lattice in the ξ'-Al-Pd-Mn.

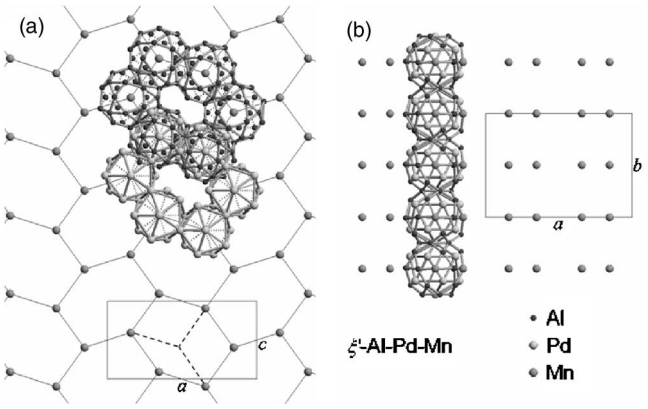

FIG. 13. (a) A view of the ξ'-Al-Pd-Mn skeleton structure[4,34] along the [0 1 0] direction. Mn atoms form a planar flattened-hexagon lattice and are located in the centers of pseudo-Mackay icosahedra. The two interpenetrating polyhedra that form the outer shell of the pseudo-Mackay cluster [a 12-atom Pd icosahedron (white atoms), and a 30-atom Al icosidodecahedron (black atoms)] are shown. The orthothombic unit cell is also shown and one of the flattened hexagons is divided into a Penrose tiling by dashed lines. (b) The same structure viewed along [0 0 1]. There are two planes of flattened hexagons at $y=0$ and $1/2$ in the unit cell.

The sample material was grown by the Bridgman technique (for details see Ref. 7). A monocrystalline sample was shaped in the form of a rectangular prism with dimensions $1.8\times1.6\times5$ mm^3 and the long axis pointed along the [0 1 0] direction (that represents the pseudotenfold symmetry axis of the structure). Its composition was determined with EDXS to be $Al_{73}Pd_{22.9}Mn_{4.1}$. The structural quality and the physical properties (electrical resistivity, magnetism, thermal conductivity, and thermoelectric power) of this sample are reported elsewhere[6] (in Ref. 6, this sample is labeled as ξ'-AlPdMn-1). The results confirm that the sample is a structurally homogeneous single-phase monocrystal. The sample possesses the following physical properties:[6] electrical resistivity is temperature-independent within 2% between room temperature and 4 K with the value $\rho_{300\ \mathrm{K}}=213\ \mu\Omega$ cm; magnetic susceptibility χ is diamagnetic, containing a small Curie contribution with an estimated fraction $f\approx7\times10^{-5}$ of paramagnetic Mn atoms and the thermoelectric power is small and negative, amounting to $-6\ \mu$V/K at room temperature.

B. Orientation-dependent ^{27}Al NMR spectra

Similarly to the previously analyzed β-Al_3Mg_2 and $Mg_{32}(Al,Zn)_{49}$ Bergman-phase crystals, the ^{27}Al NMR spectrum of monocrystalline ξ'-$Al_{73}Pd_{22.9}Mn_{4.1}$ shows the structure of a narrow central line and a broad satellite intensity [Fig. 14(a)], but is otherwise featureless and powderlike. The satellite intensity extends over an interval of 5 MHz, which is much broader than in the other two compounds. In Fig. 14(a), two frequency-swept spectra recorded at $T=80$ K in a magnetic field 6.34 T and angles $\beta=18°$ and 36° are displayed for the rotation about the [0 1 0] direction. As before, $\beta=0$ corresponds to the field parallel to [1 0 0]. We observe

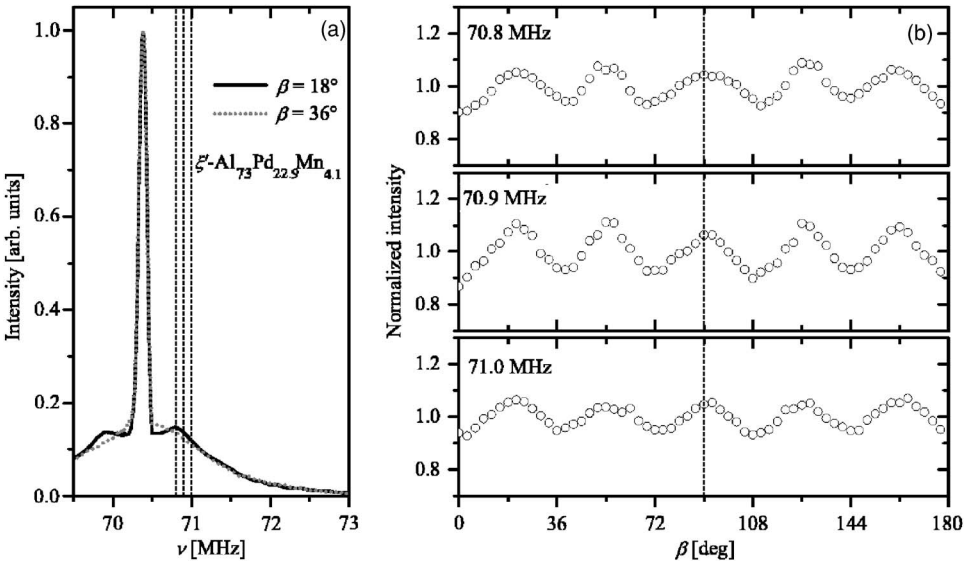

FIG. 14. (a) ^{27}Al frequency-swept NMR spectra of monocrystalline ξ'-$Al_{73}Pd_{22.9}Mn_{4.1}$ at $T=80$ K in a magnetic field 6.34 T and angles $\beta=18°$ and 36°. Vertical dashed lines indicate the frequencies at which the window-intensity rotation patterns were recorded. (b) Rotation patterns of the window intensity in the rotation about the [0 1 0] pseudotenfold direction at the selected frequencies 70.8, 70.9, and 71.0 MHz.

that the orientation-dependent variation of the NMR intensity in the satellite part is tiny, but we shall show that it is still large enough to yield significant rotation patterns of the window intensities. Since the electrical resistivity of the ξ'-$Al_{73}Pd_{22.9}Mn_{4.1}$ is a factor 5–7 larger than those of β-Al_3Mg_2 and the Bergman phase, its Knight shift is expected to be considerably smaller than in the other two compounds, so that it can again be neglected when analyzing the orientation-dependent first-order quadrupole-perturbed satellite intensity. The rotation patterns of the window intensity in the rotation about [0 1 0] were recorded at frequencies 70.8, 70.9, and 71.0 MHz [indicated in Fig. 14(a) by vertical dashed lines] and are displayed in Fig. 14(b). All three rotation patterns exhibit five maxima between 0 and 180° separated by 36°, indicating a pseudotenfold $2\pi/10$ symmetry. This is in agreement with structural considerations,[4] where individual atomic layers of ξ'-Al-Pd-Mn exhibit local pentagonal symmetry, whereas adjacent layers are rotated by 36° about [0 1 0] with respect to each other, so that the unit cell obeys the symmetry of a pseudotenfold screw axis. However, while the rotation pattern at 71.0 MHz exhibits five peaks of equal height (indicating an almost-perfect tenfold-rotation symmetry), the rotation pattern at 70.9 MHz exhibits four peaks of equal height, whereas the central peak at $\beta=90°$ is slightly lower than the other four. One can still claim that this rotation pattern exhibits an approximate (pseudo) tenfold symmetry, but one can also consider that this is a twofold-symmetric pattern with mirror symmetry around $\beta=90°$. Likewise, the pattern at 70.8 MHz can be regarded loosely as a pseudotenfold symmetric or, more precisely, as a twofold symmetric. The rotation patterns in Fig. 14(b) hence reveal that the [0 1 0] axis of the ξ'-Al-Pd-Mn structure is close to a tenfold screw axis (therefore a *pseudo*tenfold axis), but in reality it is only a twofold symmetry axis of the structure.

In a theoretical calculation of the EFG distribution using the structural data of the Boudard model,[4] the *ab initio* approach was beyond our computational capabilities (too many atoms in the unit cell and the many partially occupied or vacant sites in the structure). On the other hand, we could still perform the *ab initio* calculation to determine atomic valences that were used in the subsequent point-charge calculation (we obtained dimensionless charges $q_{Al}=0.3\pm0.1$, $q_{Pd}=-0.6\pm0.2$, and $q_{Mn}=-0.7\pm0.2$). Similarly to β-Al_3Mg_2, we have filled the unit cell first with the atoms at fully occupied sites and then added the atoms on partially occupied sites by a random-generation procedure, taking into account the shortest-distance criterion. The problems arose from (i) the many Al sites with Al/vacancy substitutional disorder, as the omission of one atom has changed the EFG tensor drastically and (ii) the fact that more than half of the 320 atomic sites in the unit cell are fractionally occupied. We nevertheless conducted the point-charge calculation, but the rotation patterns of the theoretical window intensities (not shown) always showed a predominant twofold-symmetry character and did not give good fits of the experimental ones. In Fig. 15(a), the theoretical distribution of the orientations of the V_{ZZ} principal axis on the sphere viewed along the [0 1 0] direction is shown. We observe the predominant twofold symmetry of the pattern with traces of tenfold symmetry. This is in qualitative agreement with the symmetry of the experimental rotation patterns in Fig. 14(b). The theoretical marginal distributions $f(V_{ZZ})$ and $r(\eta)$ are displayed in Figs. 15(b) and 15(c). In contrast to the discretelike distributions of β-Al_3Mg_2 and the Bergman phase, the two marginal distributions of the ξ'-Al-Pd-Mn are smooth and continuous, demonstrating the existence of a large continuous manifold of crystallographically different sites in the unit cell due to structural and substitutional disorder. The crystalline nature of the structure is still clearly manifested in Fig. 15(a), where the orientational distribution of the V_{ZZ} principal axis exhibits a well-ordered nonrandom pattern. As no quantitative agreement between the theory and the experiment could be obtained, we conclude that the point-charge model is inadequate in the case of ξ'-Al-Pd-Mn, very likely due to the same reason as for the Bergman phase (the charge of conduction electrons is considered to be confined to lattice points instead of being smeared over the unit cell).

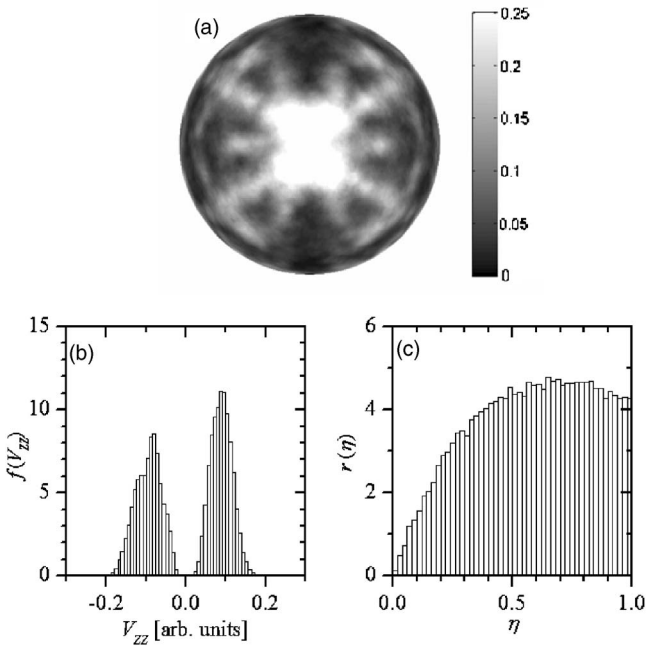

FIG. 15. (a) Theoretical distribution of the orientations of the V_{ZZ} principal axis on the sphere viewed along the [0 1 0] crystalline direction, calculated for the structural model of ξ'-Al-Pd-Mn by Boudard.[4] A twofold-symmetric pattern is observed with traces of tenfold symmetry (ten equally spaced radial directions of the intensity can be noticed). The corresponding theoretical marginal distributions (b) $f(V_{ZZ})$ and (c) $r(\eta)$ are also shown.

VI. CONCLUSIONS

We conducted a ^{27}Al NMR study of three giant-unit-cell CMA compounds, β-Al_3Mg_2, the Bergman-phase $Mg_{32}(Al,Zn)_{49}$, and ξ'-Al-Pd-Mn, all in the monocrystalline form. The ^{27}Al NMR spectra are strongly inhomogeneously broadened predominantly by the electric quadrupole interaction. The spectral intensities extend over several MHz, so that field-sweep and frequency-sweep techniques are needed to record the spectra. The spectral shapes of all the investigated compounds are featureless and powderlike, apart from the trivial spin $I=5/2$ structure of a narrow central line and broad satellite intensity. Rotating the crystals in a magnetic field, the spectra do not shift with orientation but exhibit variation of the intensity on the satellite part of the spectrum. Measuring orientation-dependent satellite intensity in appropriate frequency windows yields significant rotation patterns that reveal the macroscopic symmetry of the unit cell. For a theoretical reproduction of the window-intensity rotation patterns, a distribution of the EFG tensors was calculated from the existing structural models. The ^{27}Al spectrum was then calculated in an orientation-dependent manner and the window intensity was extracted and compared to the experimental patterns. Matching of the experimental and theoretical patterns then yields a distribution of the EFG tensors in the unit cell both in magnitude and orientation. This distribution carries important structural information on the manifold of different local atomic environments in the unit cell and distinguishes crystallographically inequivalent lattice sites (characterized by EFG tensors with different eigenvalues) from equivalent sites that possess the same EFG eigenvalues, but are rotated in space according to the symmetry of the space group. The distribution of the EFG tensors in the unit cell is the final achievement of our NMR investigation, providing important structural information for the CMA compounds with giant unit cells, comprising from several hundred up to more than a thousand atoms. It is surprising that so rich information can be obtained from the tiny orientation dependence of the satellite intensity of the NMR spectra.

In the theoretical calculation of the EFG distribution for the 1168-atom unit cell of β-Al_3Mg_2, a point-charge calculation performed on the structural model by Samson[11] was successful and yielded good matching of the experimental and theoretical window-intensity rotation patterns that obey the fourfold symmetry of the space group $Fd\bar{3}m$. Due to the known problems of the point-charge calculation for metallic solids (the EFG contribution due to conduction electrons is treated improperly), this success is somewhat surprising. It seems that the giant size of the unit cell acts in favor of the point-charge model. Another possibility, still to be considered, is that the conduction electrons in β-Al_3Mg_2 exhibit partial localization on atomic clusters, making them more point-chargelike.

For the $Mg_{32}(Al,Zn)_{49}$ Bergman phase with 160 atoms in the unit cell of the Sun model,[17] the point-charge approach turned out to be inadequate, whereas the *ab initio* calculation of the atomic-charge distributions and the EFG tensors reproduced well the rotation patterns of the NMR window intensity. Despite the cubic form of the Bergman-phase unit cell, the rotation patterns and the distribution of the EFG orientations obey the twofold symmetry of the space group $Im\bar{3}$ that contains no fourfold-rotation symmetry element. The marginal distribution $f(V_{ZZ})$ is composed of three "sticks" and confirms that the giant unit cell of the Bergman phase possesses only three ^{27}Al EFG tensors with different eigenvalues and thus three crystallographically inequivalent Al sites.

In our last example, the ξ'-Al-Pd-Mn with 258 atoms in the unit cell, the *ab initio* calculation was not feasible due to too many atoms in the unit cell and the many fractionally occupied sites that also exhibit substitutional Al/vacancy disorder. A point-charge calculation could still be performed, but yielded predominantly twofold-symmetric patterns of the window intensity, in contrast to the experimental ones that showed the symmetry of a pseudotenfold axis. No good matching between the theory and experiment could be obtained, showing inadequacy of the point-charge model in the case of ξ'-Al-Pd-Mn. A further refinement of the existing structural model of ξ'-Al-Pd-Mn would also be desirable.

To conclude, we believe that the above-presented investigation of the orientation-dependent NMR spectra can serve as a reference for future NMR studies of the giant-unit-cell intermetallics, showing that valid structural information can be extracted from the NMR spectra that are extremely inhomogeneously broadened and their shapes appear to be

hopelessly simplified, featureless, and powderlike at a first glance. Good-quality monocrystalline samples are needed for such studies, which is a complicated crystal-growing task by itself in the context of newly emerging CMA materials.

ACKNOWLEDGMENT

This work was done within the activities of the sixth Framework EU Network of Excellence "Complex Metallic Alloys" (Contract No. NMP3-CT-2005-500140).

[1] See, for a review, K. Urban and M. Feuerbacher, J. Non-Cryst. Solids **334&335**, 143 (2004).
[2] G. Bergman, J. L. T. Waugh, and L. Pauling, Acta Crystallogr. **10**, 254 (1957).
[3] F. J. Edler, V. Gramlich, and W. Steurer, J. Alloys Compd. **269**, 7 (1998).
[4] M. Boudard, H. Klein, M. de Boissieu, M. Audier, and H. Vincent, Philos. Mag. A **74**, 939 (1996).
[5] H. Klein, M. Audier, M. Boudard, M. de Boissieu, L. Behara, and M. Duneau, Philos. Mag. A **73**, 309 (1996).
[6] J. Dolinšek, P. Jeglič, P. J. McGuiness, Z. Jagličić, A. Bilušić, Ž. Bihar, A. Smontara, C. V. Landauro, M. Feuerbacher, B. Grushko, and K. Urban, Phys. Rev. B **72**, 064208 (2005).
[7] M. Feuerbacher, C. Thomas, and K. Urban, in *Quasicrystals, Structure and Physical Properties*, edited by H.-R. Trebin (Wiley-VCH, Weinheim, 2003), p. 2.
[8] G. Kreiner and H. F. Franzen, J. Alloys Compd. **261**, 83 (1997).
[9] L. Pauling, J. Am. Chem. Soc. **45**, 2777 (1923).
[10] L. Pauling, Am. Sci. **43**, 285 (1955).
[11] S. Samson, Acta Crystallogr. **19**, 401 (1965).
[12] S. Samson, in *Developments in the Structural Chemistry of Alloy Phases*, edited by B. C. Giessen (Plenum, New York, 1969), p. 65.
[13] R. Cerny, M. Francois, K. Yvon, D. Jaccard, E. Walker, V. Petricek, I. Cisarova, H.-U. Nissen, and R. Wessiken, J. Phys.: Condens. Matter **8**, 4485 (1996).
[14] See, e.g., C. Janot, *Quasicrystals*, 2nd ed. (Clarendon, Oxford, 1994).
[15] C. L. Henley and V. Elser, Philos. Mag. B **53**, L59 (1986).
[16] C. Janot, *Quasicrystals*, 2nd ed. (Clarendon, Oxford, 1994), p. 112.
[17] W. Sun, F. J. Lincoln, K. Sugiyama, and K. Hiraga, Mater. Sci. Eng., A **294–296**, 327 (2000).
[18] See, e.g., J. Winter, *Magnetic Resonance in Metals* (Oxford, Clarendon Press, 1971), Chaps. II, IV, and V.
[19] P. Jeglič and J. Dolinšek, Phys. Rev. B **71**, 014204 (2005).
[20] H. L. Su, M. Harmelin, P. Donnadieu, C. Baetzner, H. J. Seifert, H. L. Lukas, G. Effenberg, and F. Aldinger, J. Alloys Compd. **247**, 57 (1997).
[21] M. Feuerbacher, M. Heggen, and K. Urban, Mater. Sci. Eng., A **375–377**, 84 (2004).
[22] J. Dolinšek, T. Apih, P. Jeglič, I. Smiljanić, A. Bilušić, Ž. Bihar, A. Smontara, Z. Jagličić, M. Heggen, and M. Feuerbacher (unpublished).
[23] G. Czjzek, J. Fink, F. Götz, H. Schmidt, J. M. D. Coey, J.-P. Rebouillat, and A. Liénard, Phys. Rev. B **23**, 2513 (1981).
[24] See, for a review, G. Le Caër and R. A. Brand, J. Phys.: Condens. Matter **10**, 10715 (1998).
[25] R. A. Brand, G. Le Caër, and J. M. Dubois, J. Phys.: Condens. Matter **2**, 6413 (1990).
[26] D. A. Petrov, in *Ternary Alloys*, edited by G. Petzow and G. Effenberg (VCH Publishers, Weinheim/New York, 1993), Vol. 7, p. 57.
[27] T. Takeuchi and U. Mizutani, Phys. Rev. B **52**, 9300 (1995).
[28] U. Mizutani, W. Iwakami, T. Takeuchi, M. Sakata, and M. Takata, Philos. Mag. Lett. **5**, 34 (1997).
[29] A. Smontara, I. Smiljanić, A. Bilušić, Z. Jagličić, M. Klanjšek, J. Dolinšek, S. Roitsch, and M. Feuerbacher, J. Alloys Compd. (to be published).
[30] J. P. Perdew and Y. Wang, Phys. Rev. B **45**, 13244 (1992).
[31] P. Blaha, K. Schwarz, and P. Herzig, Phys. Rev. Lett. **54**, 1192 (1985).
[32] P. Blaha, K. Schwarz, P. Sorantin, and S. B. Trickey, Comput. Phys. Commun. **59**, 399 (1990).
[33] E. Wimmer, H. Krakauer, M. Weinert, and A. J. Freeman, Phys. Rev. B **24**, 864 (1981).
[34] L. Beraha, M. Duneau, H. Klein, and M. Audier, Philos. Mag. A **76**, 587 (1997).